M3D-C1 simulations of the plasma response to RMPs in NSTX-U single-null and snowflake divertor configurations

IOP Publishing | International Atomic Energy Agency Nuclear Fusion

Nucl. Fusion **57** (2017) 076007 (12pp) https://doi.org/10.1088/1741-4326/aa6e10

M3D-C1 simulations of the plasma response to RMPs in NSTX-U single-null and snowflake divertor configurations

G.P. Canal[1,2], N.M. Ferraro[3], T.E. Evans[1], T.H. Osborne[1], J.E. Menard[3], J.-W. Ahn[4], R. Maingi[3], A. Wingen[4], D. Ciro[5], H. Frerichs[6], O. Schmitz[6], V. Soukhanoviskii[7], I. Waters[6] and S.A. Sabbagh[8]

[1] General Atomics, PO Box 85608, San Diego, CA 92186-5608, United States of America
[2] Oak Ridge Associated Universities, Oak Ridge, TN 37831, United States of America
[3] Princeton Plasma Physics Laboratory, Princeton, NJ 08543-0451, United States of America
[4] Oak Ridge National Laboratory, Oak Ridge, TN 37831, United States of America
[5] Department of Applied Physics, University of São Paulo, São Paulo, SP 05508-090, Brazil
[6] Department of Engineering Physics, University of Wisconsin—Madison, Madison, WI 53706, United States of America
[7] Lawrence Livermore National Laboratory, Livermore, CA 94550, United States of America
[8] Department of Applied Physics and Applied Mathematics, Columbia University, New York, NY 10027, United States of America

E-mail: canalg@fusion.gat.com

Received 28 September 2016, revised 17 March 2017
Accepted for publication 19 April 2017
Published 16 May 2017

Abstract

In this work, single- and two-fluid resistive magnetohydrodynamic calculations of the plasma response to $n = 3$ magnetic perturbations in single-null (SN) and snowflake (SF) divertor configurations are compared with those based on the vacuum approach. The calculations are performed using the code M3D-C[1] and are based on simulated NSTX-U plasmas. Significantly different plasma responses were found from these calculations, with the difference between the single- and two-fluid plasma responses being caused mainly by the different screening mechanism intrinsic to each of these models. Although different plasma responses were obtained from these different plasma models, no significant difference between the SN and SF plasma responses were found. However, due to their different equilibrium properties, magnetic perturbations cause the SF configuration to develop additional and longer magnetic lobes in the null-point region than the SN, regardless of the plasma model used. The intersection of these longer and additional lobes with the divertor plates are expected to cause more striations in the particle and heat flux target profiles. In addition, the results indicate that the size of the magnetic lobes, in both single-null and snowflake configurations, are more sensitive to resonant magnetic perturbations than to non-resonant magnetic perturbations.

Keywords: snowflake divertor, RMP, plasma response, two-fluid MHD

(Some figures may appear in colour only in the online journal)

1. Introduction

The high confinement mode (H-mode) is seen as the most promising operational regime for obtaining economically attractive fusion power plants based on the tokamak concept. This regime is characterized by the formation of a very steep plasma pressure profile at the plasma edge, which leads to repetitive instabilities known as 'edge localized modes' (ELMs). These instabilities have been identified as ideal magnetohydrodynamic (MHD) modes triggered by the increased plasma pressure gradient and/or current density in the plasma edge [1–4]. The crash of these modes releases a significant fraction of the

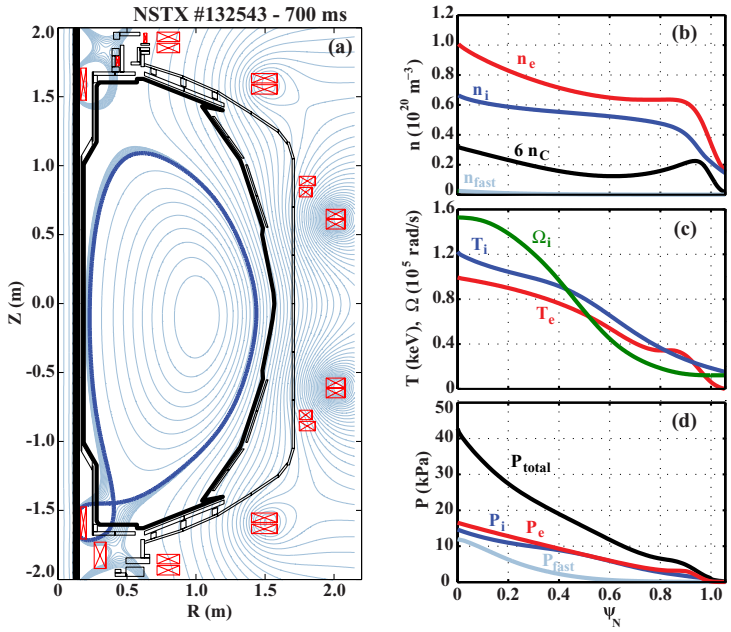

Figure 1. (*a*) Poloidal cross-section of NSTX with poloidal flux contours from the SN reference discharge #132543 at 700 ms. (*b*) Electron, ion, carbon and neutral beam injected fast particle densities. (*c*) Toroidal ion angular rotation and electron and ion temperatures. (*d*) Electron, ion, neutral beam injected fast particle, and total plasma pressures. Light blue contours around the primary separatrix in (*a*) illustrate the expected SOL width $\lambda_{q,\mathrm{us}} = 3$ mm.

plasma thermal energy into the plasma scrape-off layer (SOL) that can lead to unacceptably high transient heat fluxes onto the divertor targets [5]. The erosion caused by these bursts of energy can reduce significantly the lifetime of the plasma-facing components (PFCs) thus driving the need for ELM control in large devices such as ITER. Several experimental, numerical and theoretical studies worldwide have demonstrated that the presence of relatively small non-axisymmetric resonant magnetic perturbations, created by currents flowing in non-axisymmetric coils outside the plasma, can be used to suppress ELMs [6]. The results from these studies led to the addition of ELM control coils to the ITER baseline design [7].

To demonstrate a sustained burning plasma operation with fusion power gain factor $Q \geqslant 10$, while preserving the integrity of the PFCs, ITER will have to rely on a high fraction of power exhausted through radiation. In the demonstration power plant (DEMO) that is planned to follow ITER, and in future fusion power plants, this fraction is expected to be of the order of 95% [8, 9]. However, it is still unclear if these conditions can be achieved in reactor-sized machines while maintaining operation in the H-mode [9].

To mitigate the risk that highly radiating regimes may not extrapolate towards devices like DEMO, several alternative magnetic divertor configurations, such as the snowflake (SF), have been proposed and are being researched. The SF divertor is characterized by a second order null-point, an hexagonal structure with four divertor legs, and a lower poloidal magnetic field in the vicinity of the null-point compared to a conventional single-null (SN) divertor [10–12]. In practice, however, the SF configuration features two nearby first order null-points instead, since the currents in the poloidal field coils always differ slightly from those required for creating an exact SF configuration. In such SF configurations, the primary x-point determines the last closed flux surface (LCFS) while the secondary one can be located either in the private flux region of the primary separatrix, usually referred to as snowflake plus (SF+), or in its common flux region, usually referred to as snowflake minus (SF−). Due to its lower poloidal magnetic field in the null-point region, the SF configuration is expected to have a larger flux expansion in the vicinity of the null-point, larger divertor volume and a longer connection length.

Several machines have demonstrated experimentally the feasibility of the SF divertor, namely the TCV tokamak [13, 14], the NSTX spherical torus [15–17] and the DIII-D tokamak [18]. Experiments in these devices have shown that the SF configuration leads to a substantial decrease of the peak heat flux on the divertor plates. In addition, it facilitates the access to detachment while keeping the energy confinement, L–H threshold and H-mode pedestal height similar to those obtained in similarly shaped SN diverted plasmas [14, 16, 18].

The ELM control coils and the snowflake divertor are two potential solutions that have been proposed to solve two separate outstanding issues on the path towards self-sustained burning plasma operations. In a reactor, these two solutions would have to operate simultaneously and, therefore, it is important to investigate whether these solutions are compatible and can operate simultaneously without major conflicts. In this work, the effect of externally applied magnetic perturbations on the SF divertor configuration is investigated on NSTX-U through numerical simulations. This article is organized as follows: section 2 describes a series of NSTX-U SF + equilibria with various distances between primary and secondary x-points. Before perturbing these SF equilibria with non-axisymmetric magnetic fields, this set of equilibria is characterized and discussed in

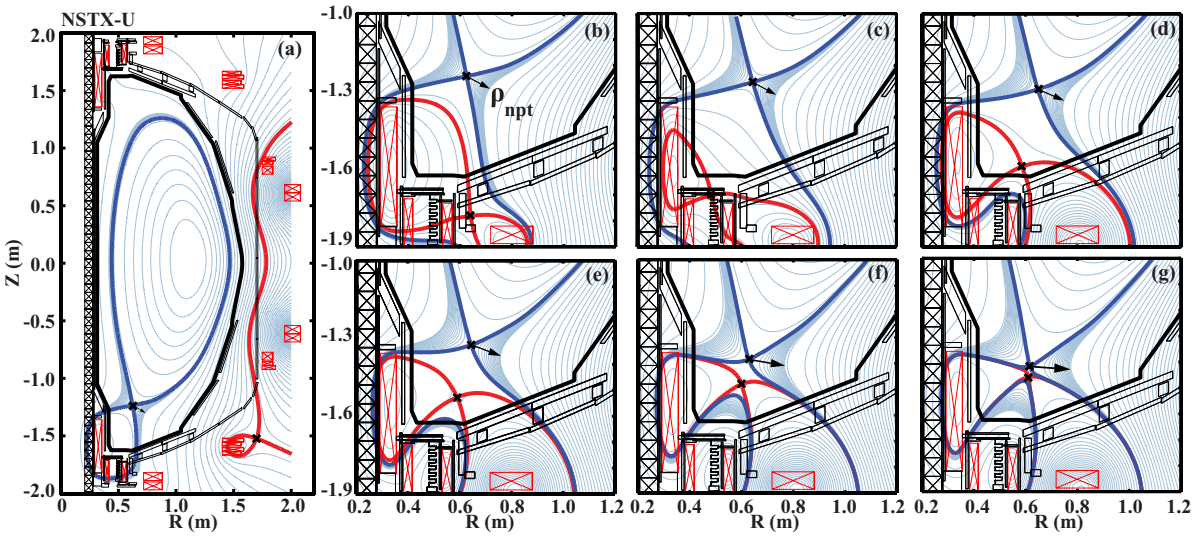

Figure 2. Poloidal cross-section of NSTX-U with poloidal flux contours from (*a*) a SN configuration ($d_{\mathrm{xpts}} = 110$ cm) and from the series of SF+ equilibria with various distances between primary and secondary x-points: (*b*) $d_{\mathrm{xpts}} = 54$ cm, (*c*) $d_{\mathrm{xpts}} = 46$ cm, (*d*) $d_{\mathrm{xpts}} = 30$ cm, (*e*) $d_{\mathrm{xpts}} = 21$ cm, (*f*) $d_{\mathrm{xpts}} = 10$ cm and (*g*) $d_{\mathrm{xpts}} = 4.4$ cm. Blue and red curves correspond to primary and secondary separatrices. Light blue contours around the primary separatrix illustrate the expected SOL width $\lambda_{q,\mathrm{us}} = 3$ mm.

section 3, where the effect of the divertor configuration on the main SOL features is presented. Section 4 presents the physical model of the M3D-C^1 code used to model the plasma response to the applied magnetic perturbations. Section 5 presents single- and two-fluid resistive MHD calculations of the linear response to magnetic perturbations of NSTX-U plasmas in both SN and SF configurations. The results from these two plasma models are compared with those obtained without the plasma response and the differences between the results from these two plasma models are discussed. Section 6 presents the effect of the divertor configuration on the manifolds (magnetic lobes) calculated using single- and two-fluid resistive MHD models and the results are compared with those without considering the plasma response. The main results are summarized in section 7.

2. NSTX-U SF configurations

A series of NSTX-U SF+ equilibria, with various distances between primary and secondary x-points, was created to evaluate the influence of the divertor configuration on the geometrical properties of the SOL. These equilibria were created with the free-boundary equilibrium code ISOLVER [19] using the plasma kinetic profiles and global plasma parameters from a typical single-null NSTX ELM-y H-mode discharge (#132543), figure 1. In this NSTX discharge, the global plasma parameters were: minor radius $a = 0.57$ m, elongation $\kappa = 2.1$, top triangularity $\delta_{\mathrm{top}} = 0.36$, bottom triangularity $\delta_{\mathrm{bot}} = 0.71$, safety factor at 95% and 97% of the normalized poloidal flux $q_{95} = 7.4$ and $q_{97} = 8.6$, total input power $P_{\mathrm{in}} = 6.2$ MW, plasma current $I_{\mathrm{p}} = 1.1$ MA, toroidal magnetic field $B_0 = 0.43$ T and $\beta_{\mathrm{N}} = 4.8$.

To generate the NSTX-U configurations, the plasma boundary and the position of strike points, x-points, and magnetic axis, were all adjusted by varying the PF coil currents in order to move the primary x-point far from the wall to have more space to vary the distance between primary and secondary x-points with the secondary x-point inside the vacuum vessel. The distance between the two nearby x-points in these equilibria was decreased from approximately $d_{\mathrm{xpts}} = 110$ cm to 4.4 cm, figure 2. The location of the primary x-point was not set to optimize divertor performance but to well separate the null-point region from the divertor targets. To take advantage of the increased flux expansion, the null-point region should be placed relatively closer to the divertor targets.

A recent scaling for the SOL width at the upstream position, $\lambda_{q,\mathrm{us}}$, was obtained from regression in a multi-machine database for inter-ELM heat flux measurements in attached H-mode plasmas [20]. Using the plasma parameters from the NSTX reference discharge, this scaling predicts a $\lambda_{q,\mathrm{us}} \approx 3$ mm for this series of NSTX-U SF+ equilibria. This expected value for the SOL width is represented in figures 1(*a*) and 2 by light blue flux contours around the primary separatrix.

3. Geometrical properties of the NSTX-U SF equilibria

One of the main features of an exact SF configuration is that not only the magnitude of the poloidal magnetic field, B_θ, at the primary x-point vanishes but also its gradient, $|\vec{\nabla} B_\theta|_{\mathrm{xpt}}$. The value of $|\vec{\nabla} B_\theta|_{\mathrm{xpt}}$ is thus a measure that indicates the proximity of a divertor configuration to an exact SF. The value of $|\vec{\nabla} B_\theta|_{\mathrm{xpt}}$ for the SF+ configuration with the shortest distance between x-points, $|\vec{\nabla} B_\theta|_{\mathrm{xpt}} = 0.061\,\mathrm{T\,m^{-1}}$, is about 5 times smaller than for the SN, $|\vec{\nabla} B_\theta|_{\mathrm{xpt}} = 0.33\,\mathrm{T\,m^{-1}}$. The proximity of a divertor configuration to an exact SF can also be parametrized by σ, defined as the distance between the two nearby x-points, d_{xpts}, normalized to the plasma minor radius, a, figure 3. For values of $\sigma \gtrsim 1.0$, the secondary x-point does not affect the poloidal

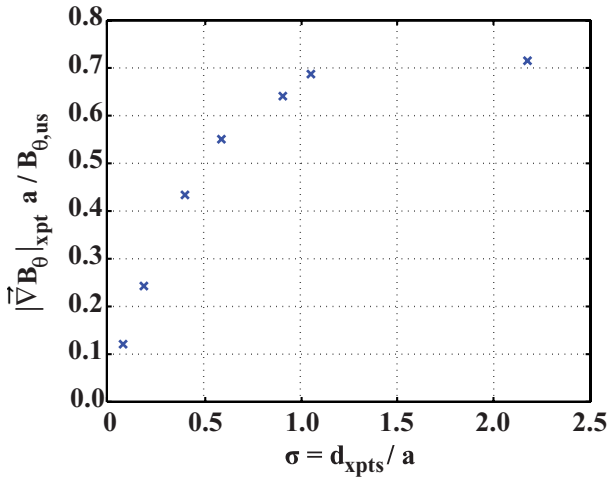

Figure 3. Gradient of the magnitude of the poloidal magnetic field at the primary x-point, $|\vec{\nabla}B_\theta|_{\rm xpt}$, normalized to $B_{\theta,\rm us}/a$, as a function of σ.

field distribution near the primary x-point and, therefore, any NSTX-U divertor configuration with $\sigma \gtrsim 1.0$ is expected to behave as a SN divertor. In this work, the SN configuration ($\sigma \approx 2.2$) is used as a reference to evaluate the modifications in the SOL geometrical properties caused by changes in the divertor configuration.

The SOL geometrical properties used here to characterize the NSTX-U divertor configuration are the smallest magnitude of the poloidal magnetic field on a flux surface in the vicinity of the primary x-point, $B_{\theta,\rm npt}$, the minimum distance of a flux surface to the primary x-point, $\rho_{\rm npt}$, which is closely related to the divertor volume, and the connection length, $L_{\parallel,\rm t}$, here defined as the length of a magnetic field line between the upstream position and the outermost strike point on the divertor target. The radial dependencies of these SOL properties are shown in figure 4 with the radial coordinate being the distance from the LCFS at the upstream position, $\rho_{\rm us}$.

The magnitude of $B_{\theta,\rm npt}$ is found to decrease as σ is reduced. This causes the value of $\rho_{\rm npt}$ to exceed that of the SN for the entire SOL width by more than 50%. This indicates that the NSTX-U SF configuration is expected to take advantage of a significantly larger divertor volume, which is usually associated with larger radiative losses and greater energy transfer to neutrals [21].

Higher values of $L_{\parallel,\rm t}$ are usually associated with lower electron temperature at the divertor target and easier access to detachment [21]. The results show that, in the SF configuration, only about one third of the SOL close to the separatrix ($\rho_{\rm us} \lesssim 1.1$ mm) experiences a longer $L_{\parallel,\rm t}$ than that in a SN configuration, while the outer part of the SOL has approximately the same geometrical properties in both configurations. Previous experiments on NSTX, however, showed that the SF configuration facilitates access to detachment [16]. Assuming that both NSTX and NSTX-U have similar SOL features, it is noteworthy that the advantageous effects of the SF configuration are noticeable experimentally even though only a small part of the SOL in the immediate vicinity of the separatrix has all the properties associated with a SF. This result agrees with

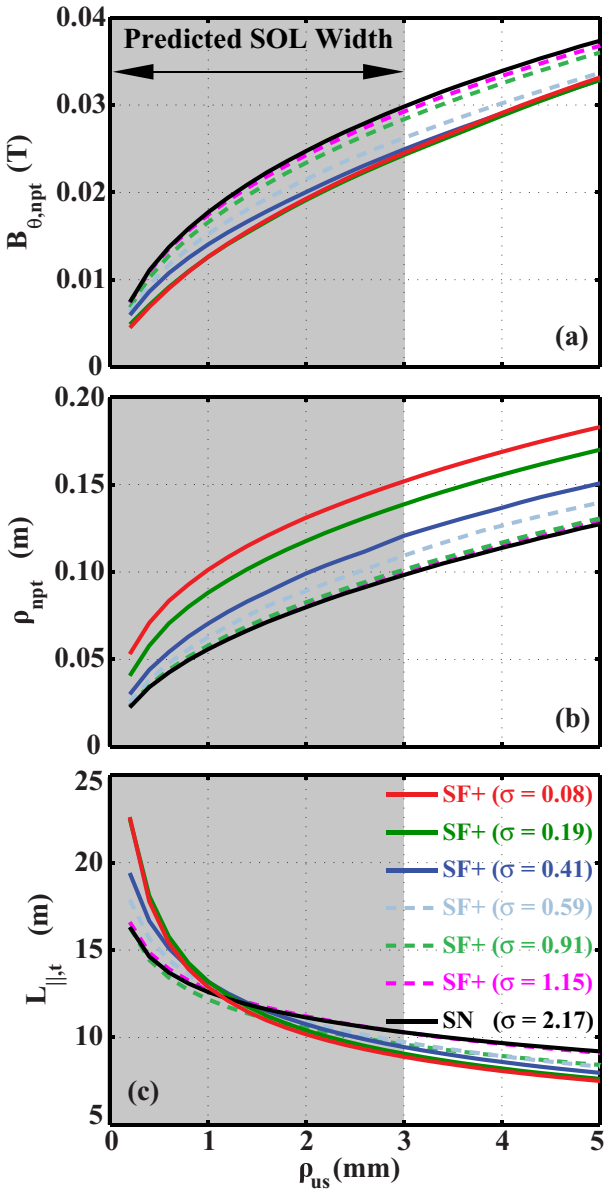

Figure 4. Radial dependencies of the SOL geometrical properties of the set of SF+ equilibria with various values of σ as a function of the upstream coordinate $\rho_{\rm us}$. (*a*) Smallest magnitude of the poloidal field in the vicinity of the primary x-point. (*b*) Minimum distance of a flux surface to the primary x-point. (*c*) Connection length between upstream position and the outermost strike point. The shadows represent the expected value for the SOL power fall-off length $\lambda_{q,\rm us} = 3$ mm.

previous studies, which show that in medium-sized machines, such as NSTX, NSTX-U and the TCV tokamak, the enhancement of the SOL properties are predicted to be limited to the inner part of the SOL close to the separatrix [22]. In DEMO-sized machines, however, the SF properties are expected to be significantly enhanced across the entire SOL. Note that even though the SF configurations created in present machines are not expected to have all the geometrical properties enhanced across the entire SOL [22], significant changes of the cross-field transport in the null-point region of the SF divertor,

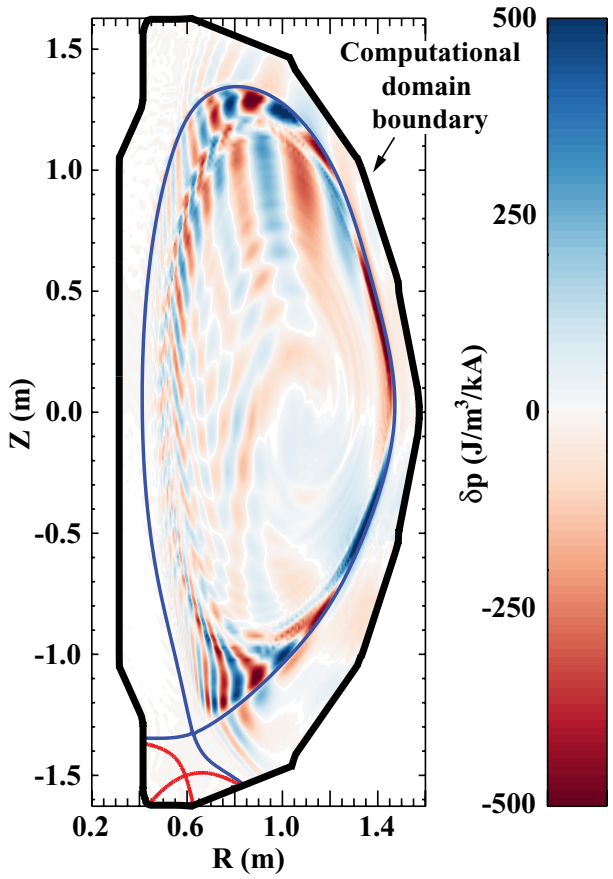

Figure 5. Perturbation of the total plasma pressure from the two-fluid plasma response to an externally applied $n = 3$ magnetic perturbation.

compared to that in a SN configuration, have been observed [22–24]. Several mechanisms have been proposed to account for these experimental observations, such as stronger $\vec{E} \times \vec{B}$ in the null-point region [25] and triggering of a so-called 'churning mode' [26, 27], among others [28].

4. The M3D-C^1 code

M3D-C^1 is a code developed to study various plasma phenomena of interest to controlled thermonuclear fusion [29] and, in this work, it is used to estimate the plasma response to applied non-axisymmetric magnetic perturbations.

The M3D-C^1 code is a parallel, finite-element code capable of calculating the solution of resistive single-fluid and two-fluid MHD equations in diverted, toroidal geometry [30]. Here the capability of M3D-C^1 is used to solve a set of time-independent equations, namely

$$\vec{\nabla} \cdot (n\vec{v}_\mathrm{i}) = 0, \tag{1}$$

$$m_\mathrm{i} n \vec{v}_\mathrm{i} \cdot \vec{\nabla}\vec{v}_\mathrm{i} = \vec{J} \times \vec{B} - \vec{\nabla} p - \vec{\nabla} \cdot \mathbf{\Pi}_\mathrm{i}, \tag{2}$$

$$\frac{\vec{\nabla} \cdot (p\vec{v}_\mathrm{i})}{\Gamma - 1} + p\vec{\nabla} \cdot \vec{v}_\mathrm{i} + \vec{\nabla} \cdot \vec{q} = \eta J^2 - \mathbf{\Pi}_\mathrm{i} : \vec{\nabla}\vec{v}_\mathrm{i} - \frac{\vec{J}}{ne(\Gamma - 1)} \cdot \left(\Gamma p_\mathrm{e} \frac{\vec{\nabla} n}{n} - \vec{\nabla} p_\mathrm{e} \right), \tag{3}$$

$$\vec{\nabla} \times \vec{E} = 0, \tag{4}$$

$$\vec{\nabla} \times \vec{B} = \mu_0 \vec{J}, \tag{5}$$

$$\vec{E} = \eta \vec{J} - \vec{v}_\mathrm{i} \times \vec{B} + \frac{1}{ne}(\vec{J} \times \vec{B} - \vec{\nabla} p_\mathrm{e}), \tag{6}$$

where $\vec{v}_\mathrm{i}$ is the ion fluid velocity, p_e and p the electron and total plasma pressures, $\vec{J}$ the electric current density, $\vec{B}$ the magnetic field, $\vec{E}$ the electric field,

$$\mathbf{\Pi}_\mathrm{i} = -\mu_\mathrm{i} [\vec{\nabla}\vec{v}_\mathrm{i} + (\vec{\nabla}\vec{v}_\mathrm{i})^\mathrm{t}] \tag{7}$$

the ion viscosity tensor and

$$\vec{q} = -\kappa \vec{\nabla}(T_\mathrm{e} + T_\mathrm{i}) - \kappa_\parallel \vec{B}(\vec{B} \cdot \vec{\nabla} T_\mathrm{e})/B^2, \tag{8}$$

the heat flux, which accounts for isotropic and parallel heat conduction transport.

In these calculations, quasi-neutrality is assumed ($n_\mathrm{e} = n_\mathrm{i} = n$), the electron and ion temperatures are defined as $T_{\mathrm{e,i}} = p_{\mathrm{e,i}}/n$, m_i is the ion mass, here assumed to be that of deuterium, Γ is the ratio of specific heats, here assumed to be equal to 5/3, η is the Spitzer electric resistivity, κ and $\kappa_\parallel$ are the isotropic and parallel heat conductivities, with $\kappa_\parallel/\kappa = 10^6$, and μ_i the isotropic ion viscosity. Both κ and μ_i are kept constant across the computational domain at values $\kappa = 1.5 \times 10^{20}$ m^{-1} · s^{-1} and $\mu_\mathrm{i} = 5.2 \times 10^{-7}$ kg · m^{-1} · s^{-1}, such that at the top of the total pressure pedestal, where $n_\mathrm{i} \approx 5.0 \times 10^{19}$ m^{-3}, the heat and momentum diffusivities are, respectively, $\chi = \kappa/n_\mathrm{i} \approx 3.0$ m^2 s^{-1} and $\eta_\mathrm{i} = \mu_\mathrm{i}/(m_\mathrm{i} n_\mathrm{i}) \approx 3.1$ m^2 s^{-1}.

In this work, only the linear plasma response is considered, such that n, $p_{\mathrm{e,i}}$, $\vec{v}_\mathrm{i}$, $\vec{J}$, $\vec{B}$ and $\vec{E}$ are separated into equilibrium and perturbed components, e.g. $n = n_0 + \delta n$, and only the linear perturbed terms are retained. The perturbed part of the magnetic field includes both the applied magnetic perturbation and the plasma response. In the system of linearized equations, the electron and ion perturbed pressures are assumed to be half of the total perturbed pressure, $\delta p_\mathrm{e} = \delta p_\mathrm{i} = \delta p/2$. This assumption is found to significantly improve the computational efficiency without affecting the results significantly.

In the calculations presented in this work, the six NSTX-U non-axisymmetric midplane coils, usually referred as resistive wall mode, error field (RWMEF) coils [31, 32], are used to create the magnetic perturbations and are modelled as curved rectangles extending exactly 60° in the toroidal direction. The magnetic perturbations have $n = 3$ toroidal periodicity with 1 kA of current circulating in each coil. The perturbed magnetic field produced by these currents is calculated using Biot-Savart law and, therefore, all the toroidal harmonics up to $n = 18$ (determined by the finite grid spacing in the toroidal direction) generated by these coils were taken into account in these calculations.

To solve the system of linearized equations, a perfectly conducting wall is assumed at the computational domain boundary and, therefore, the sum of the equilibrium and

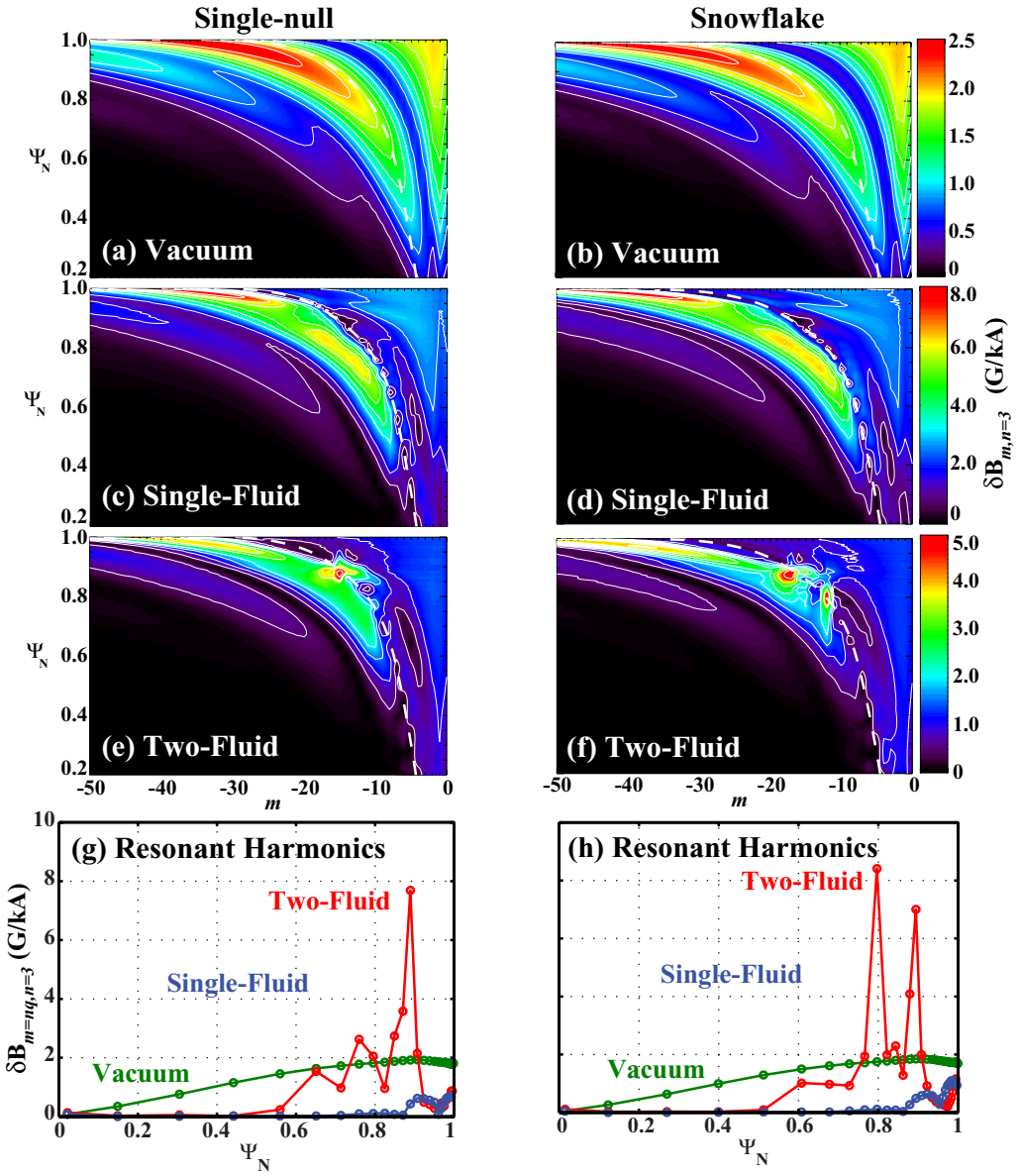

Figure 6. Poloidal Fourier spectrum of the perturbed magnetic field normal to the unperturbed flux surfaces ((*a*)–(*b*)) without plasma response, and ((*c*)–(*d*)) with single- and ((*e*)–(*f*)) two-fluid plasma responses in the NSTX-U SN and SF configurations. ((*g*)–(*h*)) Amplitude of the poloidal Fourier harmonics along the resonant condition $m = 3q$ indicated by the white dashed lines in ((*a*)–(*f*)).

applied magnetic perturbations is held fixed along the boundary domain. The perturbed quantities, however, are forced to vanish at the computational boundary, here taken to be the NSTX-U inner wall, figure 5.

In the two-fluid M3D-C^1 model, the electron and ion fluid velocities are distinguished and, in these calculations, the equilibrium ion fluid velocity is assumed to be entirely toroidal,

$$\vec{v}_i = R\,\Omega_i\,(\Psi)\hat{e}_\phi, \tag{9}$$

with Ω_i being the toroidal ion angular rotation and R the radial coordinate. The equilibrium electron fluid velocity, however, has both toroidal and poloidal components,

$$\vec{v}_e = R\omega_e(\Psi)\hat{e}_\phi + \frac{K(\Psi)}{n}\vec{B}, \tag{10}$$

with $\omega_e(\Psi)$ and $K(\Psi)$ being flux surface functions that depend on equilibrium parameters [33]. Note that the flux surface averaged electron angular rotation perpendicular to the magnetic field,

$$\langle\Omega_{e,\perp}\rangle = \langle\frac{\vec{v}_e}{R}\cdot\frac{\vec{B}_0\times\vec{\nabla}\Psi}{|\vec{B}_0\times\vec{\nabla}\Psi|}\rangle = \langle\frac{B_\theta}{B}\rangle\omega_e(\Psi), \tag{11}$$

is proportional to ω_e, which is distinct from the flux surface averaged toroidal electron angular rotation,

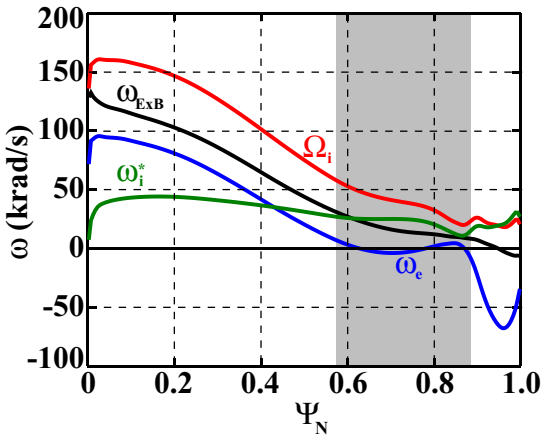

Figure 7. Radial profiles of ion (red), electron (blue), ion diamagnetic (green) and $\vec{E} \times \vec{B}$ (black) angular rotations in the SN configuration. No significant difference between the plasma rotation components in the SN and SF configurations is observed. The shadow indicates the region of low electron angular rotation.

$$\langle \Omega_{e,\phi} \rangle = \langle \frac{\vec{v}_e \cdot \hat{e}_\phi}{R} \rangle = \omega_e(\Psi) + \langle \frac{B_\phi}{Rn} \rangle K(\Psi). \qquad (12)$$

In M3D-C[1], the single-fluid model is recovered by omitting the last term of equations (3) and (6), which constraints the electron and ion fluid velocities to be the same and both equal to the $\vec{E} \times \vec{B}$ velocity.

5. Effect of the divertor configuration on the plasma response

In this section, the effect of the divertor configuration on the plasma response to applied $n = 3$ magnetic perturbations is investigated. To evaluate the changes in the plasma response associated to the SF divertor, the linear plasma response of the SN configuration is used as a reference. Due to the sensitivity of the SF configuration to fluctuations of the shaping coil currents, values of σ as low as 0.1 are usually achieved only transiently during experiments. Therefore, to evaluate effects that can be observed within the experimental limits, a SF+ configuration with $\sigma = 0.3$ will be used in these calculations. The single- and two-fluid plasma responses in both SN and SF configurations are calculated and compared with calculations assuming no plasma response, usually referred to as the 'vacuum approach'.

The vacuum approach calculations provide almost identical results for both SN and SF configurations and predict a significantly broader spectrum of poloidal Fourier harmonics near the plasma edge than in the plasma core region, which is just a consequence of the radial multi-pole decay of the poloidal harmonics generated by the $n = 3$ perturbations. This can be seen in figures 6((*a*)–(*b*)), which show the amplitudes of the poloidal harmonics of the perturbed magnetic field normal to the unperturbed flux surfaces computed by the SURFMN code [34] using

$$\delta B_{m,n} = \frac{(2\pi)^2}{A} \int_0^{2\pi} \int_0^{2\pi} \frac{\delta \vec{B} \cdot \vec{\nabla} \psi}{\vec{B} \cdot \vec{\nabla} \theta^*} e^{-i(m\theta^* - n\phi)} d\theta^* d\phi, \qquad (13)$$

where $\delta \vec{B}$ is the amplitude of the total magnetic perturbation, which is the sum of the applied magnetic perturbation and the plasma response, $\vec{B}$ is the equilibrium magnetic field, A is the poloidal surface area of the magnetic flux surface of interest, m is the poloidal mode number, ϕ is the toroidal angle and θ^* is the straight-line magnetic field angle, such that $d\theta^* = q^{-1} d\phi$. The negative values of the harmonics along the resonant condition $m = qn$ (dashed white lines in figures 6((*a*)–(*f*))) indicate that the plasma has left-hand helicity, which is caused by the opposite signs of the plasma current and toroidal magnetic field relative to each other. The finite amplitude of the tearing (resonant) components along the resonant condition, figures 6((*a*)–(*b*) and (*g*)–(*h*)), indicates the formation of magnetic islands that, depending on their width, can overlap creating a region of stochastic magnetic field lines. The calculations also show kink (non-resonant) components with $m > nq$ concentrated close to the plasma edge.

The plasma response from the single-fluid calculations, however, show a significant screening of the tearing components across the plasma with respect to the vacuum approach, with a strong amplification of the non-resonant kink components $m/n = 12/3$ and $m/n = 17/3$ and also some components with higher values of m near the plasma edge, figures 6((*c*)–(*d*) and (*g*)–(*h*)). Note the different ranges of values in the color scale of this figure. No significant differences between SN and SF configurations are found in the vacuum and single-fluid calculations.

The two-fluid calculations for both SN and SF configurations show a substantial screening of the tearing components in the plasma edge, with respect to the vacuum approach but, in contrast to the single-fluid results, a significant amplification of the tearing components is found at the $q = 17/3$ rational surface for the SN and at both the $q = 12/3$ and $17/3$ rational surfaces for the SF, figures 6((*e*)–(*f*) and (*g*)–(*h*)). The non-resonant kink components in both the SN and SF configurations are significantly smaller than those in the single-fluid calculations.

The different plasma responses obtained from the single- and two-fluid calculations are caused by the different screening mechanisms of these two plasma models. The screening of external magnetic perturbations is always caused by the electron rotation but, in the single-fluid model, the electron rotation is equal to the $\vec{E} \times \vec{B}$ rotation while, in the two-fluid model, diamagnetic rotation also affects the screening. In the single-fluid calculations, the $\vec{E} \times \vec{B}$ rotation is sufficiently large across the plasma to prevent the perturbations from penetrating, except at the plasma edge, where the $\vec{E} \times \vec{B}$ plasma rotation reverses its direction, figure 7.

Concerning the two-fluid model, theoretical [35] and numerical [33, 36] studies have shown that the penetration of external magnetic perturbations into the plasma is predominantly determined by the electron fluid rotation perpendicular to $\vec{B}$, $\Omega_{e,\perp}$. Consistent with these previous results, the two-fluid calculations in both SN and SF configurations show an amplification of the tearing components in the region of low ω_e and a screening in the regions of high ω_e, figures 6((*g*)–(*h*)) and 7. The amplification of the 12/3 tearing component in the

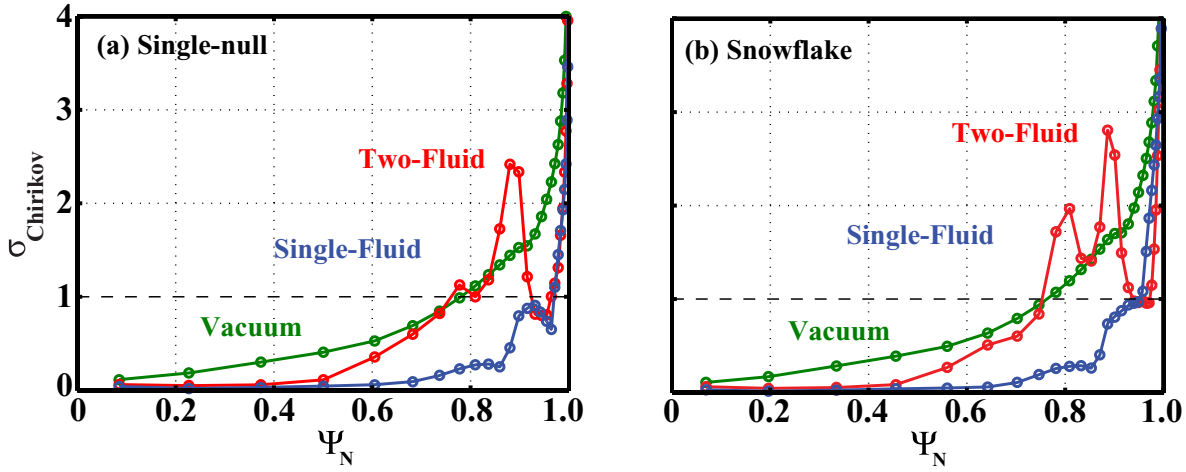

Figure 8. Chirikov parameter calculated for (*a*) SN and (*b*) SF configurations without accounting for the plasma response (vacuum) and with single- and two-fluid plasma responses taken into account.

SF configuration, in addition to the 17/3 tearing component, is due to a slight change of the q profile that moves the $q = 12/3$ rational surface closer to the position where ω_e vanishes. Although different plasma responses were obtained from the single- and two-fluid calculations, no significant differences between the SN and SF plasma responses were found.

6. Effect of the divertor configuration on the magnetic lobes

In a perfectly axisymmetric diverted plasma configuration, the equilibrium separatrix associated to an x-point is composed by a stable and an unstable manifold that perfectly overlay. When non-axisymmetric magnetic fields perturb such an axisymmetric configuration, however, the stable and unstable manifolds do not overlay and complex topological structures known as homoclinic tangles arise from the intersection between these manifolds [37]. The manifolds oscillate and increase their excursions as they asymptotically approach the x-point, forming structures commonly called 'magnetic lobes'. The manifolds act as the plasma boundary and, in such non-axisymmetric configuration, field lines from inside the perturbed plasma volume can connect to the targets through intersections of the magnetic lobes with the target plates. The splitting of the separatrix into two manifolds generates stochastic magnetic fields. In Hamiltonian systems, such as magnetically confined plasmas, the onset of stochasticity can be qualitatively described by a criterion based on the overlapping of magnetic islands [38–40],

$$\sigma_{\text{Chirikov}} = \frac{\Delta\psi_{m,n} + \Delta\psi_{m+1,n}}{2|\psi_{m+1,n} - \psi_{m,n}|} \gtrsim \sigma_c, \qquad (14)$$

where σ_{Chirikov} is the so-called Chirikov parameter and $\sigma_c \approx 1$ a critical value that might take values lower than unit depending on the field configurations. This criterion states that a stochastic region will form between two neighbouring magnetic islands when the distance between them $\delta\psi = |\psi_{m+1,n} - \psi_{m,n}|$ becomes smaller than their average island width $\Delta\psi = (\Delta\psi_{m,n} + \Delta\psi_{m+1,n})/2$.

This criterion indicates that, in the single-fluid model, the significantly reduced, but still finite, tearing components in both SN and SF configurations lead to the formation of a stochastic region for $\Psi_N \gtrsim 0.95$, figure 8, where the stochastic field lines can escape the plasma and connect to the divertor plates through intersections of the magnetic lobes with the target plates. In the two-fluid model, however, the stochastic region extends inward into the region where $\omega_e \approx 0$, figure 7. The edge stochasticity ($\Psi_N \gtrsim 0.95$) calculated using both single- and two-fluid models is expected to be the same for the SN configuration and is significantly smaller than in the vacuum approach, figure 8(*a*). In the SF configuration, the edge stochasticity is also significantly smaller than in the vacuum approach, but a slightly higher stochasticity is expected in the single-fluid response than for the two-fluid, figure 8(*b*). This slight difference can be seen in figure 9, which shows the connection length of field lines started in a rectangular grid and followed using the field line tracing code TRIP3D-MAFOT [32, 41, 42]. These TRIP3D-MAFOT calculations also show that the size of the stochastic layer in the plasma edge, for both single- and two-fluid plasma responses, are about the same in the SN configurations and are smaller than that from the vacuum approach, figures 9((*a*)–(*c*)), while for the SF, the stochastic layer is slightly smaller in the two-fluid compared with that in the single-fluid model and vacuum approach, figures 9((*d*)–(*f*)).

To study the effect of the divertor configuration on the structure of the magnetic lobes, the manifolds in both SN and SF configurations were also calculated using TRIP3D-MAFOT and are shown by the black contours in figure 9. The calculations show that, regardless of the plasma model used, the SF configuration has more and longer magnetic lobes than the SN, figures 9 and 10. Note that a toroidal phase shift from the single- and two-fluid plasma responses affects the location of the lobes with respect to those from the vacuum approach calculations. Since all the toroidal harmonics up to $n = 18$ (determined by the computational grid toroidal

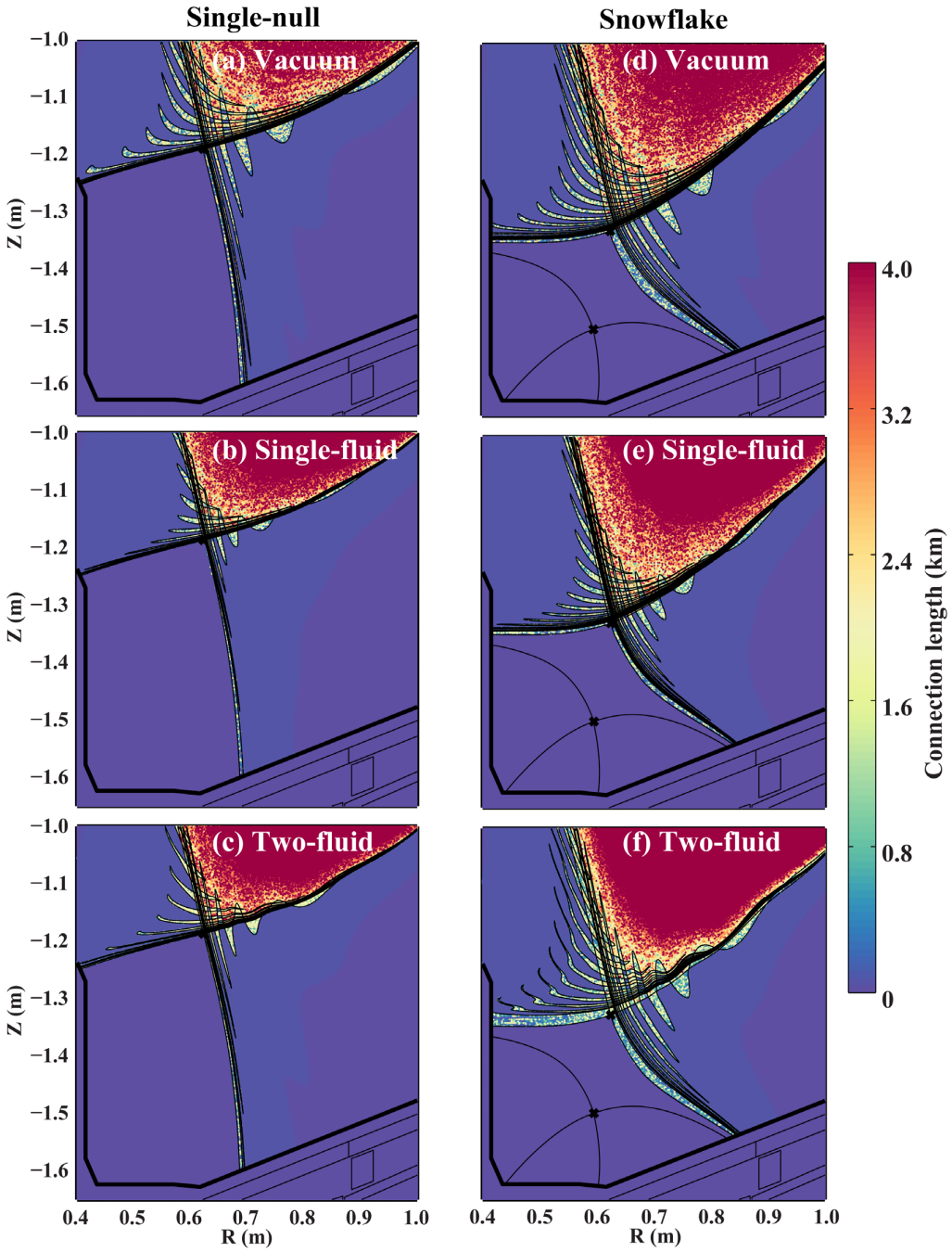

Figure 9. Connection length of magnetic field lines in the divertor region of the (*a*)–(*c*) SN and (*d*)–(*f*) SF configurations using the vacuum approach (no plasma response) and with the single- and two-fluid plasma responses.

spacing), generated by the six NSTX-U non-axisymmetric midplane coils, were taken into account, a toroidal phase shift in the plasma response can be introduced by the superposition of the individual plasma responses to each toroidal harmonic component of the RMP field, which in turn can introduce a displacement to the divertor footprints in the toroidal direction. The increase in number and size of the lobes is caused by the equilibrium flux expansion and, therefore, is observed in both single- and two-fluid plasma response calculations, and also in the vacuum approach calculations. Such an increase comes from an interplay between the conservation of the magnetic flux through the lobes and the lower B_θ in the null-point region. This interplay causes an additional compression, and a stretching, of the lobes near the x-point to preserve the magnetic flux. Field lines in the SF configuration, therefore, tend to asymptotically approach the null-point more slowly than in a SN, forcing the manifolds to oscillate more times and to develop longer magnetic lobes compared to those in the SN configuration. This also explains the larger number of magnetic lobes on the left side of the primary x-point, where

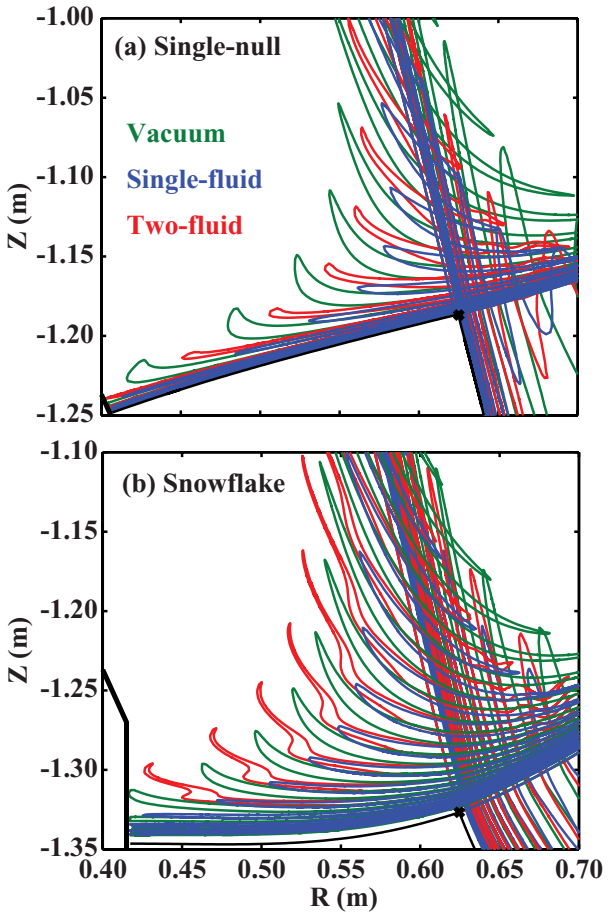

Figure 10. Manifolds of (*a*) SN and (*b*) SF configurations calculated using the vacuum approach (no plasma response) and with the single- and two-fluid plasma responses. Same data as in figure 9.

the toroidal magnetic field is stronger. The intersection of the longer and additional magnetic lobes of the SF configuration with the divertor plates are expected to cause additional striations in the particle and heat flux target profiles [45].

In the single-fluid calculations, the magnetic lobes in both the SN and SF configurations are found to be shorter than those from the two-fluid and vacuum approach calculations. In the two-fluid calculations, however, the magnetic lobes of the SN are slightly shorter than those from the vacuum approach while the lobes of the SF are slightly longer. These results correlate with the observed strong reduction of the tearing components in the single-fluid calculations, figure 6(*g*), and the strong amplification of the tearing components in the two-fluid calculations, figure 6(*h*), and suggest that the size of the magnetic lobes are more sensitive to resonant than to non-resonant magnetic perturbations. This observation is further supported by the fact that, even though the kink components of the single-fluid plasma response are the largest among the three models, being about three times larger than in the vacuum approach and about two times larger than in the two-fluid, the single-fluid plasma response produces the shortest lobes among the three models.

7. Summary

The ELM control coils and the snowflake (SF) divertor configuration are two potential solutions proposed to solve two separate outstanding issues on the path towards self-sustained burning plasma operations. These two solutions have been tested separately in several machines worldwide but, in a reactor, these two solutions would have to operate simultaneously. It is, therefore, important to investigate the compatibility between these two solutions and to identify possible conflicts that could prevent them from operating simultaneously.

In this work, single- and two-fluid resistive magnetohydrodynamic calculations of the plasma response to externally applied magnetic perturbations on single-null (SN) and SF divertor configurations are compared with those based on the vacuum approach, i.e. assuming no plasma response. For such a comparison, a series of NSTX-U SF equilibria, with various distances between primary and secondary x-points, have been generated with the free-boundary equilibrium solver ISOLVER using the plasma kinetic profiles and global plasma parameters from a typical NSTX ELMy H-mode discharge (#132543).

A characterization of the SOL geometrical properties of the unperturbed axisymmetric configurations shows that the NSTX-U SF plasmas are expected to have a significantly larger divertor volume than the single-null (SN) configuration. However, the results show that only about one third of the SOL in the vicinity of the separatrix experiences a longer connection length than that in a SN configuration, while the outer part of the SOL has approximately the same geometrical properties in both divertor configurations. It is noteworthy that the advantageous effects of the SF configuration have been observed experimentally even though only a small part of the SOL has all the properties associated with a SF.

In these simulations, the six NSTX-U non-axisymmetric midplane coils were used to create the magnetic perturbations. The coils were modelled as curved rectangles extending exactly 60° in the toroidal direction, with 1 kA of current circulating in each coil and with an $n = 3$ configuration. The perturbed magnetic field produced by these currents was calculated using Biot-Savart law and, therefore, all the toroidal harmonics up to $n = 18$ (determined by the finite grid spacing in the toroidal direction) generated by these coils were taken into account. To estimate the linear single- and two-fluid plasma responses to these magnetic perturbations on NSTX-U plasmas with SN and SF divertor configurations, the two-fluid resistive magnetohydrodynamic code M3D-C[1] was used. Note that non-linear effects, in the sense of the modification of the $n = 0$ profiles by transport from the $n > 0$ response, are expected to play an important role in the plasma response, especially through changes in plasma density and rotation profiles that result from the application of resonant magnetic perturbations (RMPs). Unfortunately these effects are beyond the capability of present MHD code models, even when solving the full set of non-linear equations, since they do not include the physics that determines the edge transport (neoclassical and microturbulence). This is a general limitation of reduced models used in both ideal and resistive MHD

codes, i.e. it is a manifestation of the present state-of-the-art on MHD modeling that needs to be addressed in the future.

The single-fluid calculations presented in the paper show a significant reduction of the resonant tearing components, with respect to the vacuum approach calculations, for both SN and SF configurations. In the two-fluid calculations, the tearing components are significantly reduced in the plasma edge and significantly amplified in the region of low electron fluid rotation perpendicular to $\vec{B}$. The differences between the single- and two-fluid plasma responses are mainly caused by the different screening mechanisms of these two plasma models. While the screening of resonant magnetic perturbations in the single-fluid model is caused by the $\vec{E} \times \vec{B}$ rotation, the screening of RMPs in the two-fluid model is caused by the local electron fluid velocity perpendicular to $\vec{B}$.

Experiments on TEXTOR [43] and DIII-D [44] tokamaks have shown that, in single-null L-mode plasmas with certain levels of RMPs, the structure of the heat deposition patterns on the divertor plates is in agreement with calculations based on the vacuum approach. However, the single- and two-fluid MHD simulations presented here indicate that, in typical NSTX-U H-mode plasmas, the experimental heat deposition patterns on the divertor plates are expected to differ significantly from those calculated using the vacuum approach. For that reason, future experiments in NSTX-U on divertor heat flux distributions will be used to validate the physics models used in the single- and two-fluid MHD simulations presented in this paper. Note, however, that although different plasma responses were obtained from the single- and two-fluid calculations with respect to the vacuum approach, no significant differences between the SN and SF plasma responses were found. Due to their different equilibrium properties, the structure of the magnetic lobes in the SF configuration were found to be significantly different from those in the SN, regardless of the plasma model used.

To evaluate the effect of the magnetic perturbations on the structure of the magnetic lobes, the manifolds in both SN and SF configurations were calculated using the field line tracing code TRIP3D-MAFOT. A comparison between the size of the magnetic lobes, and the amplitude of the kink and tearing components from the single- and two-fluid plasma response calculations, suggests that the size of the magnetic lobes is more sensitive to the resonant than to the non-RMPs. This indicates that the splitting of the separatrix into manifolds, and thus the appearance of magnetic lobes, should be observed only when RMP components are not completely shielded by the plasma. This effect will be addressed in a future work.

The results also show that, independent of the plasma response model used, the SF has more and longer magnetic lobes than the SN configuration. This increase in number and size of the lobes is caused by the equilibrium flux expansion in the null-point region and comes from the interplay between the conservation of the magnetic flux through the lobes and the lower B_θ in the null-point region of the SF configuration, which causes a stronger compression of the lobes towards the null-point and a stretching of the lobes in the null-point region. The intersection of these longer and additional magnetic lobes with the divertor plates are expected to cause more striations in the particle and heat flux target profiles, as predicted by EMC3-Eirene transport calculations [45].

Acknowledgments

This research was supported by the General Atomics Postdoctoral Research Participation Program administered by ORAU and is part of the General Atomics Collaboration on Plasma Boundary Interfaces and Macroscopic Stability at NSTX-U. This work has been supported by the US Department of Energy, Office of Science, Office of Fusion Energy Science under DOE award DE-SC0012706, DE-FC02-04ER54698, DE-AC05-06OR23100, DE-AC02-09CH11466, DE-AC05-00OR22725, DE-SC0012315, DE-SC0013911, DE-AC52-07NA27344 and DE-SC0008520. NSTX and NSTX-U data shown in this paper can be obtained in digital format using the links: https://fusion.gat.com/global/D3D_DMP and http://arks.princeton.edu/ark:/88435/dsp01ms35tc13d.

References

[1] Connor J.W. *et al* 1998 *Phys. Plasmas* **5** 2687
[2] Ferron J.R. *et al* 2000 *Phys. Plasmas* **7** 1976
[3] Snyder P.B. *et al* 2004 *Plasma Phys. Control. Fusion* **46** A131
[4] Wilson H.R. *et al* 2006 *Plasma Phys. Control. Fusion* **48** A71
[5] Loarte A. *et al* 2003 *Plasma Phys. Control. Fusion* **45** 1549
[6] Evans T.E. *et al* 2015 *Plasma Phys. Control. Fusion* **57** 123001
[7] Loarte A. *et al* 2014 *Nucl. Fusion* **54** 033007
[8] Neilson G.H. *et al* 2012 *Nucl. Fusion* **52** 047001
[9] Zohm H. *et al* 2013 *Nucl. Fusion* **53** 073019
[10] Ryutov D.D. *et al* 2007 *Phys. Plasmas* **14** 064502
[11] Ryutov D.D. *et al* 2008 *Proc. 22th Int. Conf. on Fusion Energy (Geneva)* (Vienna: IAEA) CD-ROM file IC/P4-8 (www-naweb.iaea.org/napc/physics/FEC/FEC2008/papers/ic_p4-8.pdf)
[12] Ryutov D.D. *et al* 2012 *Plasma Phys. Control. Fusion* **54** 124050
[13] Piras F. *et al* 2009 *Plasma Phys. Control. Fusion* **51** 055009
[14] Piras F. *et al* 2010 *Phys. Rev. Lett.* **105** 155003
[15] Soukhanovskii V.A. *et al* 2011 *J. Nucl. Mater.* **415** S365
[16] Soukhanovskii V.A. *et al* 2012 *Phys. Plasmas* **19** 082504
[17] Soukhanovskii V.A. *et al* 2013 *J. Nucl. Mater.* **438** S96
[18] Allen S.L. *et al* 2012 *Proc. 24th Int. Conf. on Fusion Energy (San Diego, 2012)* PD/1-2 (www-naweb.iaea.org/napc/physics/FEC/FEC2012/presentations/801_PD12.pdf)
[19] Huang J. *et al* 2005 *47th Annual APS DPP Meeting (Denver, CO, 24–28 October 2005)* GP1 045 http://meetings.aps.org/Meeting/DPP05/Event/35162
[20] Eich T. *et al* 2013 *Nucl. Fusion* **53** 093031
[21] Pitcher C.S. and Stangeby P.C. 1997 *Plasma Phys. Control. Fusion* **39** 779
[22] Reimerdes H. *et al* 2013 *Plasma Phys. Control. Fusion* **55** 124027
[23] Vijvers W.A.J. *et al* 2014 *Nucl. Fusion* **54** 023009
[24] Lunt T. *et al* 2014 *Plasma Phys. Control. Fusion* **56** 035009
[25] Canal G.P. *et al* 2015 *Nucl. Fusion* **55** 123023
[26] Ryutov D.D. *et al* 2014 *Phys. Scr.* **89** 088002

[27] Ryutov D.D. *et al* 2015 *Phys. Scr.* **90** 099501 (Corrigendum)
[28] Ryutov D.D and Soukhanovskii V.A. 2015 *Phys. Plasmas* **22** 110901
[29] Ferraro N.M. *et al* 2010 *Phys. Plasmas* **17** 102508
[30] Jardin S.C. 2004 *J. Comput. Phys.* **200** 133
[31] Sontag A.C. *et al* 2007 *Nucl. Fusion* **47** 1005
[32] Yan L. *et al* 2006 *Nucl. Fusion* **46** 858
[33] Ferraro N.M. *et al* 2012 *Phys. Plasmas* **19** 056105
[34] Schaffer M.J. *et al* 2008 *Nucl. Fusion* **48** 024004
[35] Waelbroeck F.L. *et al* 2009 *Nucl. Fusion* **49** 104025
[36] Nardon E. *et al* 2010 *Nucl. Fusion* **50** 034002
[37] Evans T.E. *et al* 2005 *J. Phys.: Conf. Ser.* **7** 174
[38] Chirikov B.V. 1960 *J. Nucl. Energy.* C **1** 253
[39] Abdullaev S.S. *et al* 2008 *Phys. Plasmas* **15** 042508
[40] Abdullaev S.S. 2014 *Magnetic Stochasticity in Magnetically Confined Fusion Plasmas* (New York: Springer) sections 8.2 and 8.3
[41] Evans T.E. *et al* 2002 *Phys. Plasmas* **9** 4957
[42] Wingen A. *et al* 2009 *Nucl. Fusion* **49** 055027
[43] Denner P. *et al* 2014 *Nucl. Fusion* **54** 064003
[44] Schmitz O. *et al* 2014 *Nucl. Fusion* **54** 012001
[45] Frerichs H. *et al* 2016 *Phys. Plasmas* **23** 062517